LAWRENCE
LIVERMORE
NATIONAL
LABORATORY

LLNL-JRNL-509653

On the elastic-plastic decomposition of crystal deformation at the atomic level

A. Stukowski, A. Arsenlis

October 31, 2011

Modelling and Simulation in Materials Science and Engineering

Disclaimer

On the elastic-plastic decomposition of crystal deformation at the atomic scale

A. Stukowski and A. Arsenlis

Lawrence Livermore National Laboratory, Livermore, CA 94550, USA

E-mail: alexander@stukowski.de

Abstract. Given two snapshots of an atomistic system, taken at different stages of the deformation process, one can compute the incremental deformation gradient field, $\mathbf{F}$, as defined by continuum mechanics theory, from the displacements of atoms. However, such a kinematic analysis of the total deformation does not reveal the respective contributions of elastic and plastic deformation. We develop a practical technique to perform the multiplicative decomposition of the deformation field, $\mathbf{F} = \mathbf{F}^{\mathrm{e}}\mathbf{F}^{\mathrm{p}}$, into elastic and plastic parts for the case of crystalline materials. The described computational analysis method can be used to quantify plastic deformation in a material due to crystal slip based mechanisms in molecular dynamics and molecular statics simulations. The knowledge of the plastic deformation field, $\mathbf{F}^{\mathrm{p}}$, and its variation with time can provide insight into the number, motion, and localization of relevant crystal defects such as dislocations. The computed elastic field, $\mathbf{F}^{\mathrm{e}}$, provides information about inhomogeneous lattice strains and lattice rotations induced by the presence of defects.

Submitted to: *Modelling and Simulation in Materials Science and Engineering*

1. Introduction

Elastoplasticity theory is based on the multiplicative decomposition of the total deformation gradient $\mathbf{F}$,

$$\mathbf{F} = \mathbf{F}^{\mathrm{e}}\mathbf{F}^{\mathrm{p}}, \tag{1}$$

into an irreversible (plastic) part $\mathbf{F}^{\mathrm{p}}$, and a reversible (elastic) part $\mathbf{F}^{\mathrm{e}}$ [9]. In simulation models of continuum crystal plasticity, the plastic and elastic deformation fields are typically evolved explicitly, such that both contributions are already known. In classical molecular dynamics and statics, in contrast, the total deformation is the only quantity that is considered and used in common analyses. The atomic trajectories obtained from the simulation model always reflect the combined effect of both elastic and plastic deformation, and separating both contributions is a non-trivial task.

Elastic-plastic decompositions of the total deformation gradient in atomistic simulations may prove useful in quantitative analyses, since the irreversible deformation of crystalline solids is tightly linked to crystal defects, either through their creation (stacking faults, grain boundaries etc.) or their motion (dislocations). Therefore, knowledge of the plastic deformation field, $\mathbf{F}^{\mathrm{p}}$, and its variation with time can provide quantitative insight into the number, mobility, and localization of such defects. Furthermore, the ability to calculate the fields $\mathbf{F}^{\mathrm{p}}$ and $\mathbf{F}^{\mathrm{e}}$ from atomistics would provide a direct connection of atomistic models to continuum models of crystal plasticity.

Recently, a computational analysis technique, the so-called dislocation extraction algorithm (DXA) [15], has been developed to extract all lattice dislocation lines from a snapshot of a molecular dynamics simulation and to determine their individual Burgers vectors. However, this method yields only the instantaneous shape and topology of the dislocation network in the material at a given instant. While this data enables the measurement of the lattice dislocation density (scalar and tensorial), it is inadequate to quantify the actual contribution of dislocations to plastic deformation, which is generated by their motion. The lack of correlation between successive snapshots of the obtained dislocation network makes it hard to infer the exact area swept by individual dislocation segments, and to keep track of the reactions they undergo.

All the relevant information about the motion of dislocations is, however, encoded in the atomic trajectories, which are naturally obtained from molecular dynamics simulations. In the past, rudimentary attempts were made to exploit this information. Zimmerman et al. [18] introduced an atomistic quantity known as the *slip vector*, which, derived from the initial and the final configuration of the system, describes an atom's relative motion with respect to its neighbors. A moving dislocation will leave behind a 'trail' of atoms whose slip vector is equal to the Burgers vector of the dislocation. Later, the slip vector approach was picked up by Vo et al. [17] to develop an approximate measure of the plastic strain produced by dislocations in an MD simulation: In cases where the relevant dislocation types and slip system orientations are known, one can infer the aggregated plastic slip by counting the atoms that exhibit certain slip vectors. However, this method fails to properly account for plastic strain produced by dislocation junctions, or dislocations moving on crossing glide planes, which cause non-standard slip vectors.

In the present work, we will develop a practical way of computing the plastic deformation field in a crystalline solid from the atomic trajectories obtained by molecular dynamics simulations. In contrast to the method by Vo et al. [17],

the technique described here does not require a calibration step or knowledge of the slip systems of dislocations. In particular, it yields a continuum-type tensor field representation of the plastic deformation at the atomic level, from which the macroscopic plastic strain can be easily obtained by integration.

2. The total deformation gradient field

Before turning to the elastic-plastic decomposition, we first discuss the calculation of the total deformation gradient, $\mathbf{F}$, from atomistics. The existing literature on this topic (e.g. [13, 7, 19, 11]) describes different approaches to calculating an *atomic* deformation gradient, that is, a deformation gradient defined at the atomic sites. In general, the value of $\mathbf{F}$ at the location of an atom can be obtained from its relative motion with respect to nearby neighbor atoms. The existing methods mostly differ in the way these neighbors are picked and how their contributions to the $\mathbf{F}$ at the central atom are weighted.

For our purposes, however, we will pick up an idea first published by Mott et al. [11], which yields a *continuum* tensor field from the displacements of atoms using a Delaunay tessellation of space. As opposed to the atomic deformation tensors mentioned above, such a deformation gradient field is defined at all points in space (except at the atomic sites themselves). This will enable us to exactly integrate the field over the simulation volume (or parts of it) to obtain a macroscopic deformation tensor. And, as will become evident later, this approach is particularly useful when it comes to decomposing the total deformation into elastic and plastic contributions.

2.1. Kinematics

Molecular dynamics (MD) and molecular statics (MS) simulations output a set of atomic trajectories, $\{\mathbf{x}_i(t)\}$, describing the motion of individual particles or atoms in a global Cartesian coordinate system. The parameter t may denote continuous time in a MD simulation, or, alternatively, the load step in a MS simulation. The displacement vector of the i-th atom is given by $\mathbf{u}_i = \mathbf{x}_i(t_1) - \mathbf{x}_i(t_0) = \mathbf{x}_i - \mathbf{X}_i$. Here, t_0 and t_1 refer to two snapshots of the atomistic system, called the initial (or reference) configuration $\mathscr{B}_0$ and the final (deformed) configuration $\mathscr{B}_1$. We require the two configurations to be holonomic to one another, meaning that the total number and the identities of atoms do not change during the time interval $t_0 \rightarrow t_1$.

Note that we do *not* assume that the reference configuration $\mathscr{B}_0$ corresponds to a perfect, undeformed state of the crystal. In fact, both configurations, $\mathscr{B}_0$ and $\mathscr{B}_1$, may be taken at any stage of the deformation simulation, and we consider the *incremental* deformation occurring in between these two snapshots.

In a continuum description, in contrast to atomistics, the displacement field $\mathbf{u} = \mathbf{x}(\mathbf{X}) - \mathbf{X}$ is defined at every material point $\mathbf{X}$ of the continuum in the reference configuration. The second-order tensor field $\mathbf{F} = \frac{\partial \mathbf{x}}{\partial \mathbf{X}} = \mathbf{I} + \frac{\partial \mathbf{u}}{\partial \mathbf{X}}$ characterizes the local deformation and rigid-body rotation the material undergoes from t_0 to t_1.

2.2. Deformation gradient field from atomistics

In atomistic simulations, the value of the displacement field $\mathbf{u}(\mathbf{X})$ is known only at the discrete atomic positions $\{\mathbf{X}_i\}$. Thus, its gradient is not defined, unless we make an assumption on the form of the continuum field at other points of space. To establish

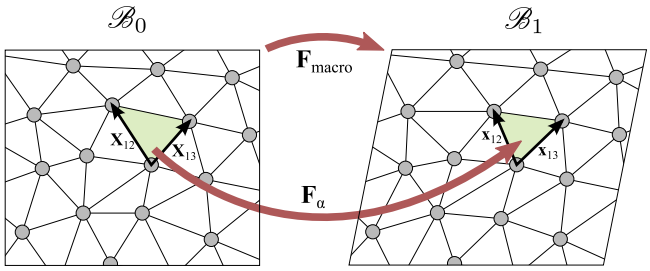

Figure 1. Schematic illustration of the calculation of the total deformation gradient field based on a space-filling tessellation of the atomistic system.

the transition to a continuum description, we assume that $\mathbf{u}(\mathbf{X})$ varies piece-wise linearly in the regions between atoms [11]. The interpolation of atomic displacement vectors is done on the basis of a space-filling decomposition into tetrahedral elements obtained from a Delaunay tessellation as shown in figure 1. In three-dimensional space, each tetrahedral element connects four atoms, and the nodal displacements obtained from molecular dynamics are interpolated linearly inside each element. Note that the Delaunay tessellation is computed only once for the reference state $\mathscr{B}_0$, and then follows the atoms as they move.

The gradient of this piece-wise linear displacement field is piece-wise constant: Within each tetrahedral element α, the deformation gradient $\mathbf{F}(\mathbf{X}) = \mathbf{F}_\alpha$ ($\mathbf{X} \in \alpha$) is homogeneous and determined exclusively by the displacement vectors of the four corner atoms. The tensor $\mathbf{F}_\alpha$ can be computed most efficiently for an element from the Cartesian coordinates of its four vertex atoms in $\mathscr{B}_0$ and $\mathscr{B}_1$, denoted by $\left\{\mathbf{X}_v^{(\alpha)}\right\}$ and $\left\{\mathbf{x}_v^{(\alpha)}\right\}$ ($v = 1 \ldots 4$) respectively. The edge vector $\mathbf{X}_{vw}^{(\alpha)} = \mathbf{X}_w^{(\alpha)} - \mathbf{X}_v^{(\alpha)}$ connects the v-th and w-th vertex of the tetrahedral element in the reference configuration, while $\mathbf{x}_{vw}^{(\alpha)} = \mathbf{x}_w^{(\alpha)} - \mathbf{x}_v^{(\alpha)}$ connects the same pair of atoms in the final configuration. The deformation gradient $\mathbf{F}_\alpha$ transforms such a line element, i.e. $\mathbf{x}_{vw}^{(\alpha)} = \mathbf{F}_\alpha \mathbf{X}_{vw}^{(\alpha)}$. We may compute $\mathbf{F}_\alpha$ from any triple of non-coplanar edges of the tetrahedral element using a product of 3×3 matrices of the form

$$\mathbf{F}_\alpha = \left[\mathbf{x}_{12}^{(\alpha)}\, \mathbf{x}_{13}^{(\alpha)}\, \mathbf{x}_{14}^{(\alpha)}\right] \cdot \left[\mathbf{X}_{12}^{(\alpha)}\, \mathbf{X}_{13}^{(\alpha)}\, \mathbf{X}_{14}^{(\alpha)}\right]^{-1}. \tag{2}$$

The resulting piece-wise constant field $\mathbf{F}(\mathbf{X})$, defined on the tetrahedral mesh, maps all edges of the tessellation from the initial to the final configuration.

Note that, in a molecular dynamics simulation at finite temperature, the deformation field will reflect the instantaneous thermal displacements of atoms. Thus, even in the absence of deformation, the computed deformation field will fluctuate at the atomic scale. If this effect is undesirable, one can take time-averaged atomic positions to compute the $\mathbf{F}_\alpha$, or coarse-grain the deformation field as discussed in the following section.

2.3. Macroscopic and mesoscopic deformation

In an MD simulation with periodic boundary conditions, the macroscopic deformation of the solid is fully determined by the affine change in shape of the simulation cell

(figure 1). We obtain the same macroscopic deformation tensor by integrating $\mathbf{F}$ over the entire simulation domain:

$$\mathbf{F}_{\mathrm{macro}} = \frac{1}{V} \int \mathbf{F} \, \mathrm{d}V, \tag{3}$$

with V denoting the volume of the simulation box in the reference configuration. Since, in our case, $\mathbf{F}$ is a piece-wise constant field, this integral can be written as a sum over all tetrahedral elements:

$$\mathbf{F}_{\mathrm{macro}} = \frac{1}{V} \sum_{\alpha} \mathbf{F}_{\alpha} V_{\alpha} = \frac{\sum_{\alpha} \mathbf{F}_{\alpha} V_{\alpha}}{\sum_{\alpha} V_{\alpha}} \tag{4}$$

The homogenized deformation of a finite region of the body (for instance a grain, or any other representative volume element) can be determined in a similar manner by restricting the sum to an adequate subset of tessellation elements. Likewise, a coarse-graining of the deformation field can be performed by projecting the volume-weighted $\mathbf{F}_{\alpha}$ values to a coarser mesh.

Note that, even though we calculated the continuous deformation field on the basis of a Delaunay tessellation, any other space-filling tessellation consisting of non-empty, non-overlapping tetrahedra would have worked too. The choice of the tessellation will affect the resulting microscopic field $\mathbf{F}$ to some extent, but the homogenized value $\mathbf{F}_{\mathrm{macro}}$ is independent of the tessellation.

Some care must be taken if atomic displacements are diffusive. Interpenetration of diffusing atoms leads to inverted tessellation elements in the deformed configuration ($\det \mathbf{F}_{\alpha} \leq 0$). However, since the integrated deformation gradient, $\mathbf{F}_{\mathrm{macro}}$, is determined by boundary displacements alone (according to the Gauss divergence theorem), the sum (4) remains valid in such a case. Furthermore, one may apply the elastic-plastic decomposition method, described in the following, to inverted elements too.

3. Separating plastic and elastic deformation

3.1. Introduction

The theory of elastic-plastic decomposition of $\mathbf{F}$ is based on the concept of a virtual intermdiate configuration of the body that is stress-free everywhere. Nemat-Nasser [12] described a hypothetical procedure for obtaining this stress-released configuration from an elastoplastically deformed configuration $\mathscr{B}$ of a continuum body: For a given point $\mathbf{x}$ in $\mathscr{B}$, consider a small neighborhood $n(\mathbf{x})$ such that the material in this neighborhood can be regarded as macroscopically homogeneous. Isolate $n(\mathbf{x})$ from the rest of $\mathscr{B}$, and release all surface tractions exerted by the rest of $\mathscr{B}$ upon $n(\mathbf{x})$ as well as all body forces on the isolated material element. Thereby we obtain the unstressed state of $n(\mathbf{x})$. Here, one makes the assumption that the unloading does not involve plastic flow. If this procedure is performed for all neighborhoods which comprise the body, one obtains the fictitious stress-released configuration $\mathscr{L}$, which is connected to the physical configuration $\mathscr{B}$ via the elastic deformation $\mathbf{F}^{\mathrm{e}}$. Note that the unstressed material patches will usually not constitute a continuous body; i.e., $\mathbf{F}^{\mathrm{e}}$ is an incompatible tangent map.

As mentioned in section 2.1, both the reference configuration $\mathscr{B}_0$ and the final configuration $\mathscr{B}_1$ may be defective states of the crystal, taken at any stage of the deformation process, and may exhibit residual and external stress fields. Let us

therefore apply the described dissection-unloading procedure to both snapshots, $\mathscr{B}_0$ and $\mathscr{B}_1$, individually. We will obtain two different stress-released configurations, $\mathscr{L}_0$ and $\mathscr{L}_1$, which are connected to the corresponding physical configurations via two elastic fields, $\mathbf{F}_0^{\mathrm{e}}$ and $\mathbf{F}_1^{\mathrm{e}}$, respectively. Here, $\mathbf{F}_0^{\mathrm{e}}$ represents the purely elastic mapping $\mathscr{L}_0 \to \mathscr{B}_0$, while $\mathbf{F}_1^{\mathrm{e}}$ describes the mapping $\mathscr{L}_1 \to \mathscr{B}_1$.

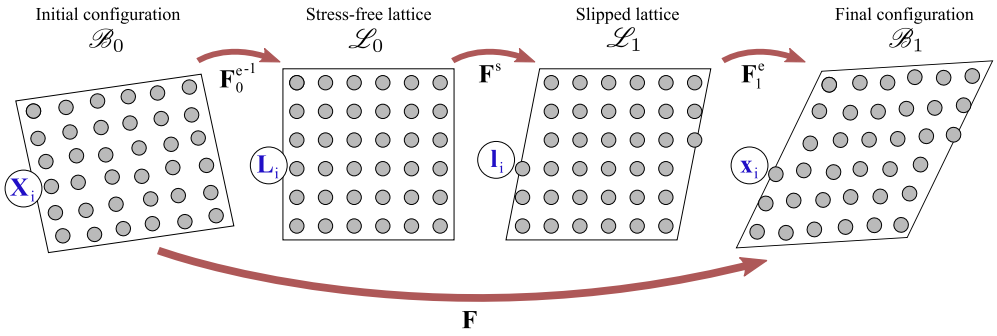

Figure 2. A representative material element undergoing both elastic and plastic deformation. The total deformation can be split up into three parts (equation 5): Two elastic fields ($\mathbf{F}_0^{\mathrm{e}}$ and $\mathbf{F}_1^{\mathrm{e}}$) that describe the deviation of the initial and final configuration from a locally stress-free state, and the plastic slip deformation, $\mathbf{F}^{\mathrm{s}}$, that connects the two stress-free configurations. Note that the two intermediate configurations are isoclinic configurations, i.e., their frame of reference is aligned with the local lattice orientation.

We now consider the stress-released states $\mathscr{L}_0$ and $\mathscr{L}_1$ as intermediate configurations and subdivide the total deformation $\mathscr{B}_0 \to \mathscr{B}_1$ (described by $\mathbf{F}$) into the sequence $\mathscr{B}_0 \to \mathscr{L}_0 \to \mathscr{L}_1 \to \mathscr{B}_1$. We then arrive at a corresponding three-term decomposition [16]

$$\mathbf{F} = \mathbf{F}_1^{\mathrm{e}} \mathbf{F}^{\mathrm{s}} \mathbf{F}_0^{\mathrm{e}-1}. \tag{5}$$

This decomposition of the total deformation is depicted in figure 2. Here we have introduced the deformation $\mathbf{F}^{\mathrm{s}}$, which connects the two intermediate configurations $\mathscr{L}_0$ and $\mathscr{L}_1$. Taking the initial configuration $\mathscr{B}_0$ as fixed, $\mathbf{F}_0^{\mathrm{e}}$ will not change with time and characterizes the initial residual strains present in $\mathscr{B}_0$. $\mathbf{F}^{\mathrm{s}}$ comprises the plastic deformation the first intermediate configuration $\mathscr{L}_0$ undergoes to arrive at the second intermediate configuration $\mathscr{L}_1$; and $\mathbf{F}_1^{\mathrm{e}}$ describes the elastic distortion of the final configuration $\mathscr{B}_1$ with respect to the associated stress-free configuration $\mathscr{L}_1$.

In our description, $\mathscr{L}_0$ and $\mathscr{L}_1$ are both *isoclinic* intermediate configurations [10]. That is, the frame of reference used to describe these virtual configurations is aligned with the local lattice structure. The tensors $\mathbf{F}_0^{\mathrm{e}}$ and $\mathbf{F}_1^{\mathrm{e}}$ both contain a rotational and a stretch component. The rotational parts reflect the local orientation of the lattice, in $\mathscr{B}_0$ and $\mathscr{B}_1$ respectively, in the global simulation coordinate system. Accordingly, they vary from grain to grain in a polycrystal. The stretch parts of $\mathbf{F}_0^{\mathrm{e}}$ and $\mathbf{F}_1^{\mathrm{e}}$ are defined by virtue of the stress release procedure and describe the initial and current local elastic strain fields in the crystalline solid due to residual and external stresses.

Since $\mathscr{L}_0$ and $\mathscr{L}_1$ are both fictitious configurations, $\mathbf{F}^{\mathrm{s}}$ has no physical meaning so far. While the elastic fields $\mathbf{F}_0^{\mathrm{e}}$ and $\mathbf{F}_1^{\mathrm{e}}$ are specified through the described dissecting and unloading procedure, $\mathbf{F}^{\mathrm{s}}$ is defined only implicitly through equation 5, i.e. $\mathbf{F}^{\mathrm{s}} = \mathbf{F}_1^{\mathrm{e}-1} \mathbf{F} \mathbf{F}_0^{\mathrm{e}}$. Since, by definition, $\mathscr{L}_0$ and $\mathscr{L}_1$ are both locally stress-free

configurations, $\mathbf{F}^{\mathrm{s}}$ must be a fully plastic deformation. We will refer to $\mathbf{F}^{\mathrm{s}}$ as the *slip deformation gradient* to distinguish it from the conventional plastic deformation gradient $\mathbf{F}^{\mathrm{p}}$ of the two-term multiplicative decomposition, equation 1.

3.2. The incremental elastic-plastic decomposition of deformation

In (computer) experiments, where a specimen is deformed by applying an external load, decomposing the total deformation into elastic and plastic fractions may be instrumental in interpreting a measured stress-strain curve or drawing conclusions on the internal processes by which deformation proceeds.

Due to the usage of isoclinic intermediate configurations in the formulation of the elastic-plastic decomposition in the preceding section, the elastic fields $\mathbf{F}_0^{\mathrm{e}}$ and $\mathbf{F}_1^{\mathrm{e}}$ directly reflect the microscopic structure of the material (including residual elastic strains and lattice orientations). For some analyses, however, the structural details of the material do not matter and only the *incremental* elastic and plastic deformation fields induced by externally applied forces are of interest. In the following we will therefore propose an alternative elastic-plastic decomposition which does not depend on the microscopic structure of the specimen.

At $t = t_0$, prior to deformation and in the absence of deformation ($\mathbf{F} = \mathbf{I}$), there can be no plastic slip. This corresponds to the initialization condition $\mathbf{F}^{\mathrm{s}}(t_0) = \mathbf{I}$, and, consequently, the current elastic field must be equal to the initial elastic field, $\mathbf{F}_1^{\mathrm{e}}(t_0) = \mathbf{F}_0^{\mathrm{e}}$. During deformation (at $t_1 > t_0$) the current elastic field, $\mathbf{F}_1^{\mathrm{e}}$, will evolve due to the applied external loads, and $\mathbf{F}^{\mathrm{s}}$ will eventually depart from identity when plastic deformation sets in. We can separate the induced elastic deformation from the preexisting residual strain at time zero by defining a new quantity, the incremental elastic deformation $\mathbf{F}^{\Delta\mathrm{e}}$, which describes only the change induced by external loads:

$$\mathbf{F}^{\Delta\mathrm{e}} = \mathbf{F}_1^{\mathrm{e}}\mathbf{F}_0^{\mathrm{e}-1}. \tag{6}$$

The corresponding incremental plastic deformation $\mathbf{F}^{\Delta\mathrm{p}}$ is obtained by requiring that the product equals the total deformation, i.e. $\mathbf{F}^{\triangle\mathrm{e}}\mathbf{F}^{\triangle\mathrm{p}} = \mathbf{F}$. From equation 5 we then get

$$\mathbf{F}^{\Delta\mathrm{p}} = \left(\mathbf{F}^{\boldsymbol{\Delta}\mathrm{e}}\right)^{-\mathbf{1}}\mathbf{F} = \mathbf{F}_0^{\mathrm{e}}\mathbf{F}^{\mathrm{s}}\mathbf{F}_0^{\mathrm{e}-1}. \tag{7}$$

The fields $\mathbf{F}^{\Delta\mathrm{e}}$ and $\mathbf{F}^{\Delta\mathrm{p}}$ are both identity at time zero, and they are independent of the frame of reference used to describe the isoclinic intermediate configurations. This makes them natural choices for measuring incremental elastic and plastic deformation in simulated experiments, in particular for the case of polycrystalline materials.

3.3. Calculation of the elastic and plastic fields

We now describe a formal way of computing the fields $\mathbf{F}_0^{\mathrm{e}}$, $\mathbf{F}_1^{\mathrm{e}}$, and $\mathbf{F}^{\mathrm{s}}$ of equation 5 at the atomic scale. Our approach is similar to the calculation of the total deformation field, $\mathbf{F}$, described in section 2.2, which we assume has already been performed. That is, a space-filling tessellation connecting all atoms in $\mathscr{B}_0$ has been generated, and each edge i-j of that tessellation has been assigned two vectors, $\mathbf{X}_{ij} = \mathbf{X}_j - \mathbf{X}_i$ and $\mathbf{x}_{ij} = \mathbf{x}_j - \mathbf{x}_i$, from which the deformation gradient in the adjacent elements is computed according to equation 2.

For now, let us suppose we were able to actually perform the hypothetical unloading procedure described in section 3.1 to determine the two intermediate

configurations. An atom i in the final configuration $\mathscr{B}_1$, located at $\mathbf{x}_i$, will move to a new position $\mathbf{l}_i$ in the intermediate configuration $\mathscr{L}_1$ upon unloading the material neighborhood surrounding it. Likewise, the same atom i, starting at $\mathbf{X}_i$ in $\mathscr{B}_0$, will move to a position $\mathbf{L}_i$ in the corresponding stress-released configuration $\mathscr{L}_0$. Given a tetrahedral element α of the tessellation, the edge vectors $\mathbf{L}_{vw}^{(\alpha)} = \mathbf{L}_w^{(\alpha)} - \mathbf{L}_v^{(\alpha)}$ and $\mathbf{l}_{vw}^{(\alpha)} = \mathbf{l}_w^{(\alpha)} - \mathbf{l}_v^{(\alpha)}$ connect two vertices v and w in the first and the second intermediate configuration respectively. The elastic-plastic decomposition for element α is then performed by computing the matrices

$$\mathbf{F}_\alpha^{\mathrm{s}} = \left[\mathbf{l}_{12}^{(\alpha)}\ \mathbf{l}_{13}^{(\alpha)}\ \mathbf{l}_{14}^{(\alpha)}\right] \cdot \left[\mathbf{L}_{12}^{(\alpha)}\ \mathbf{L}_{13}^{(\alpha)}\ \mathbf{L}_{14}^{(\alpha)}\right]^{-1} \tag{8}$$

$$\mathbf{F}_{0\alpha}^{\mathrm{e}} = \left[\mathbf{X}_{12}^{(\alpha)}\ \mathbf{X}_{13}^{(\alpha)}\ \mathbf{X}_{14}^{(\alpha)}\right] \cdot \left[\mathbf{L}_{12}^{(\alpha)}\ \mathbf{L}_{13}^{(\alpha)}\ \mathbf{L}_{14}^{(\alpha)}\right]^{-1} \tag{9}$$

$$\mathbf{F}_{1\alpha}^{\mathrm{e}} = \left[\mathbf{x}_{12}^{(\alpha)}\ \mathbf{x}_{13}^{(\alpha)}\ \mathbf{x}_{14}^{(\alpha)}\right] \cdot \left[\mathbf{l}_{12}^{(\alpha)}\ \mathbf{l}_{13}^{(\alpha)}\ \mathbf{l}_{14}^{(\alpha)}\right]^{-1}. \tag{10}$$

Note that we make use of the existing tessellation of the atomistic system, as shown in figure 3, which has been generated in the reference configuration $\mathscr{B}_0$ to calculate the field $\mathbf{F}$. Even though this tessellation was originally constructed on the basis of the atomic coordinates $\{\mathbf{X}_i\}$, it is defined exclusively by its topology, i.e. by the identities of atoms that are connected by tetrahedral elements.

The above calculation assumes that the elastic deformation within the tessellation element α is compatible and uniquely defined. In section 3.11 we will discuss the treatment of elements with incompatible elastic deformation, which are intersected by a dislocation (in either $\mathscr{B}_0$ or $\mathscr{B}_1$). Secondly, we presumed that the element is completely contained within a single material patch when the body is dissected as part of the virtual unloading procedure.

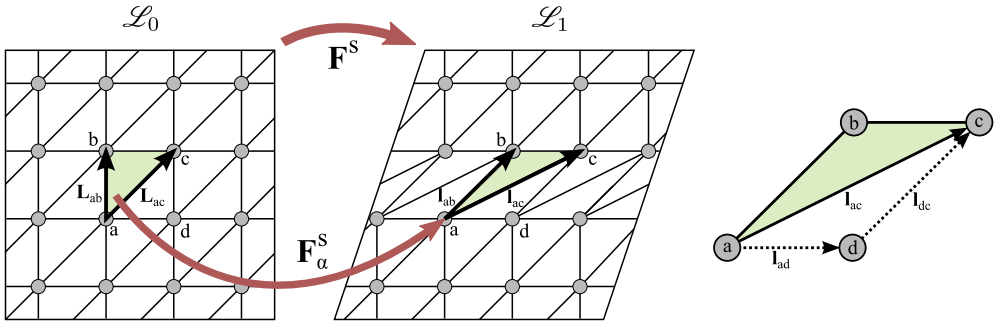

Figure 3. Schematic illustration of the plastic slip calculation in the stress-free lattice. The slip deformation gradient $\mathbf{F}_\alpha^{\mathrm{s}}$ inside a tessellation element is computed from its edge vectors before and after the plastic slip took place (equation 8). In this example, the lattice vector $\mathbf{l}_{ac}$, connecting atom a and c, cannot be determined directly since a and c are no longer direct neighbors in the deformed configuration. It must therefore be inferred from the vector sum $\mathbf{l}_{ac} = \mathbf{l}_{ad} + \mathbf{l}_{dc}$.

Equations 8–10 involve only *vectors* between atoms that are connected by a tessellation edge. It therefore boils down to developing a computational method that, given two nearby atoms i and j in the crystal, determines the connecting line elements

$\mathbf{l}_{ij} = \mathbf{l}_j - \mathbf{l}_i$ and $\mathbf{L}_{ij} = \mathbf{L}_j - \mathbf{L}_i$ in the stress-free configurations $\mathscr{L}_0$ and $\mathscr{L}_1$ (without explicitly determining $\mathbf{L}_i$,$\mathbf{L}_j$,$\mathbf{l}_i$ or $\mathbf{l}_j$).

3.4. Definition of the stress-free intermediate configurations

In the preceding section we outlined how the fields $\mathbf{F}^{\mathrm{s}}$, $\mathbf{F}_0^{\mathrm{e}}$ and $\mathbf{F}_1^{\mathrm{e}}$ can be obtained on the basis of the two stress-free intermediate configurations $\mathscr{L}_0$ and $\mathscr{L}_1$. While the total deformation gradient inside a tessellation element is fully determined by the kinematics of its four corner atoms, the decomposition into elastic and plastic parts is directly affected by our choice of the configurations $\mathscr{L}_0$ and $\mathscr{L}_1$. Therefore, we first have to define these virtual configurations more precisely before we can develop a practical way of computing them from the snapshots $\mathscr{B}_0$ and $\mathscr{B}_1$.

As mentioned in the introduction, the transitions $\mathscr{B}_0 \rightarrow \mathscr{L}_0$ and $\mathscr{B}_1 \rightarrow \mathscr{L}_1$, associated with the tangent maps $\mathbf{F}_0^{\mathrm{e}-1}$ and $\mathbf{F}_1^{\mathrm{e}-1}$, are completely equivalent. Thus, we seek a computational technique that, given an arbitrary atomistic configuration $\mathscr{B}$, yields a corresponding stress-free configuration $\mathscr{L}$. Such an algorithm can then be applied to both the initial and final configurations, $\mathscr{B}_0$ and $\mathscr{B}_1$, separately to determine the shape of a tessellation element in both relaxed configurations. In the following we denote positions and vectors in the generic physical configuration $\mathscr{B}$ with the letter $\mathbf{x}$, and corresponding positions and vectors in the associated virtual configuration $\mathscr{L}$ with the letter $\mathbf{l}$.

We start off with Nemat-Nasser's [12] hypothetical dissecting and unloading procedure, described in section 3.1, and discuss its application to defective crystals at the atomic scale. Given a point $\mathbf{x}$ in $\mathscr{B}$ (at which the elastic mapping $\mathbf{F}^{\mathrm{e}}$ is to be determined), it seems, at first glance, natural to take the tessellation element containing the point $\mathbf{x}$ as the neighborhood $n(\mathbf{x})$. By construction, the deformation of a tetrahedral element is always homogeneous. However, the material within the tessellation element is utterly inhomogeneous: All mass is concentrated in the four corner atoms. Hence, it is clear that a representative material neighborhood $n(\mathbf{x})$ must comprise more than one tessellation element, and enough atoms to appear macroscopically homogeneous. In particular, $n(\mathbf{x})$ must be large enough such that the effect of the free surfaces, created by isolating it from the rest of the body, may be neglected.

Frank [6] introduced the concept of the so-called *good* and *bad* regions that make up a crystalline material. Inside the *good* crystal regions, the lattice structure is clearly visible, and atoms are arranged on regular lattice sites. *The bad* region of a crystal comprises the cores of crystal defects, where the arrangement of atoms deviates considerably from that of the ideal lattice.

If the point $\mathbf{x}$ is located in a *good*, defect-free region of the crystal, then there is an obvious choice for the neighborhood $n(\mathbf{x})$ to be used in the stress-removal procedure: Take a group of atoms around $\mathbf{x}$ that constitute a unit cell of the lattice. Apply periodic boundary conditions to this isolated, elastically strained unit cell to model an infinite lattice with the desired homogeneous characteristics, and to avoid the effect of free surfaces that would result from the cutting operation. This unit cell will undergo a certain elastic deformation when being relaxed to the stress-free state, yielding the local elastic deformation tensor $\mathbf{F}^{\mathrm{e}-1}$ at $\mathbf{x}$. Note that, during relaxation of the unit cell's shape, atoms may undergo additional internal relaxations. Thus, the elastic deformation at the smallest level, the tetrahedral tessellation, can actually be non-uniform, even if the deformation at the unit cell level is homogeneous.

What is a good choice for the representative neighborhood $n(\mathbf{x})$ if $\mathbf{x}$ is located inside the core region of a crystal defect (the *bad* crystal region)? Two central requirements need to be fulfilled: The neighborhood, while being as small as possible, should be chosen large enough such that the contained material is macroscopically homogeneous; and the relaxation must proceed without plastic flow after removing the surface tractions from the isolated material patch. The core region of a crystal defect is, by its definition, inhomogeneous due to the lack of structural long-range order. Thus, the neighborhood $n(\mathbf{x})$ needs to be larger than the defect core in which $\mathbf{x}$ is located. On the other hand, to avoid unnecessary homogenization, $n(\mathbf{x})$ should include only a rather small amount of *good* crystal lattice around the defect, and it must not overlap with other defects embedded in the lattice. The required absence of plastic flow during relaxation of the neighborhood $n(\mathbf{x})$ implies that the defect remains in $n(\mathbf{x})$ in the stress-released configuration $\mathscr{L}$ [4]. Here, we define plastic flow as the local transition of the atomistic structure from one (sufficiently) stable configuration to another. Hence, the defect cannot dissolve during purely elastic relaxation of the isolated material patch.

It is obvious that the discussed dissection-unloading procedure has only theoretical relevance. In view of our goal to develop a useful analysis technique for atomistic computer simulations of crystalline materials, it seems unfeasible for a couple of practical reasons:

- It is not clear how the neighborhood $n(\mathbf{x})$ around a defect can be picked in an automated fashion such that the homogeneity requirement is met, in particular if the distribution of defects in the crystal is irregular and dense.
- The size of defects such as stacking faults and grain boundaries can be on the order of the system size. Then the requirement of the neighborhood $n(\mathbf{x})$ to be vanishingly small and to encompass the entire defect becomes contradictory.
- At the atomic scale, the effect of free surfaces cannot be neglected. When cutting a patch from the atomistic body, the newly created surface will inevitably introduce additional stresses, which were not present in the original material. This would change the measured elastic deformation gradient $\mathbf{F}^{\mathrm{e}-1}$ in an uncontrolled way.
- The requirement that the unloading does not trigger plastic transitions in the isolated material patch cannot be enforced in classical atomistic simulations.

3.5. A practical solution

In view of the aforementioned issues, we propose a reverse approach to obtain the mapping of atomic positions from $\mathscr{B}$ to $\mathscr{L}$: Instead of explicitly dissecting the body into small regions, and relaxing each piece individually, we start out from the relaxed states of lattices and possible defect structures and look for occurrences of these known structures in the atomistic system. Once we have found a structure in the strained crystal, we can directly compare it to the corresponding stress-free reference state to compute the local elastic deformation gradient (figure 4).

For instance, the equilibrium lattice structure of a crystalline material is usually already known, because the interatomic potential used in atomistic simulations has been explicitly fitted to reproduce this structure. Thus, it is sufficient to determine whether the atoms in the vicinity of some point $\mathbf{x}$ in $\mathscr{B}$ form this crystal structure. If yes, their relative positions in the relaxed state $\mathscr{L}$ can be predicted directly on the basis of the ideal unit cell.

In the field of atomistic computer simulations it is common practice to employ *structure identification methods* to study and visualize defects such as dislocations, stacking faults and grain boundaries in a simulated crystal. Examples for such techniques are the common neighbor analysis (CNA) [8], the bond angle analysis [2] and the centrosymmetry parameter [18]. They are used to classify the local arrangements of atoms in a simulation snapshot, and to associate them with a known reference structure. One important feature of these identification algorithms is their insensitivity to elastic distortions: The correct reference structure is still recognized, even if the actual atomic positions deviate from the corresponding ideal sites (as long as the displacements do not exceed a specific tolerance).

We will need two main ingredients for an implementation of the outlined reverse mapping approach: The first one is a catalog of lattice structures and defect structures that play a role in the atomistic simulation. It is the task of the scientist to anticipate what types of defects are present in the crystalline material or could appear during plastic deformation. In practice, the material-specific, stress-free reference state of each lattice or defect structure is determined by performing a separate static relaxation simulation as will be described below. Note that dislocation defects are explicitly excluded from this catalog for the following reason: Because our ultimate goal is to quantify the amount of plastic slip the crystal undergoes from $\mathscr{B}_0$ to $\mathscr{B}_1$, only the slipped regions of the lattice (in the wake of dislocations) are of interest. The dislocation cores themselves do not contribute to it. Moreover, the elastic field within a dislocation core is incompatible, rendering the elastic-plastic decomposition at the atomic level ambiguous (see section 3.11 for a discussion). On the contrary, stacking faults, grain boundaries, interfaces and the like play an important role for the measurement of plastic deformation, because their appearance and disappearance is directly linked to a certain amount of plastic strain.

The second ingredient is the structure identification method. Its task is to find occurrences of the reference structures in the simulation snapshot. As mentioned before, there exist efficient algorithms such as the common neighbor analysis method, which classify local atomic arrangements based on the characteristic coordination pattern of atoms. So far they were limited to simple lattices such as face-centered cubic (fcc), body-centered cubic (bcc), and hexagonal-close packed (hcp) structures. Recently, we have developed a more sophisticated analysis algorithm [14], which can also identify multi-atomic patterns and highly non-symmetric arrangements of atoms as they occur in crystal defects and lattices with larger unit cells. This pattern matching technique is flexible in terms of the structures to search for. That is, the characteristic signature of an atomic structure is not hard-coded into the algorithm, but is generated automatically on the basis of a template structure provided by the user. For an in-depth discussion of these techniques we refer the reader to [14].

The described reverse approach is depicted schematically in figure 4: First the physical configuration $\mathscr{B}$ is decomposed into discrete regions, each matching to one of the reference patterns in the structure catalog. Then the elastic field is computed from the displacements of atoms from their ideal positions in the matching template structure.

3.6. The structure catalog

In practice, the required catalog of template structures is obtained by performing a static relaxation simulation for each lattice and defect type:

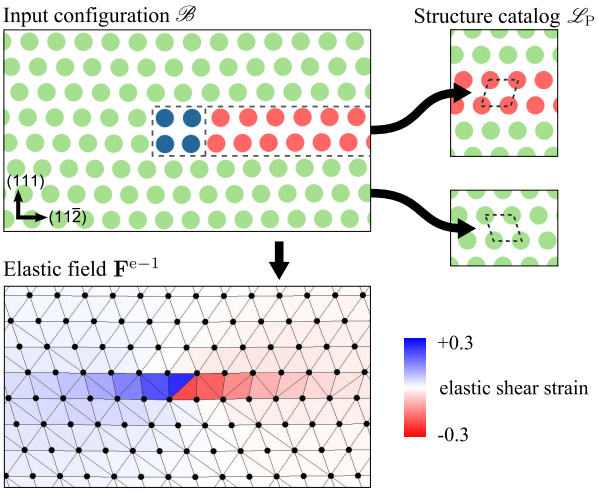

Figure 4. Calculation of the elastic deformation field in a defective crystal. Pictures on the left show a cross-section of an fcc crystal containing a stacking fault bounded by a Shockley partial dislocation. The structure catalog contains two reference patterns: the perfect fcc lattice and the infinite stacking fault core (both being macroscopically stress-free). The structure identification algorithm divides the input configuration $\mathscr{B}$ into regions, each matching to one of the ideal pattern templates. The elastic field in the defective crystal is then obtained from a local comparison of the physical atomic positions to that of the corresponding reference structure.

(i) For a crystal lattice structure, we prepare a simulation box containing a single lattice unit cell. Periodic boundary conditions are employed, and the cell shape as well as the internal degrees of freedom are relaxed until a state of zero stress is reached.

(ii) In the case of point-like defects such as vacancies, interstitials and small incoherent inclusions, we set up a large simulation box (with periodic boundary conditions) that is completely filled with the parent lattice and contains a single such defect. The box is made large enough such that elastic interactions between periodic images of the defect can be neglected.

(iii) For planar defects having a periodic structure such as stacking faults, coincidence-site-lattice (CSL) grain boundaries and other coherent crystal interfaces we use a simulation box that is long in the direction perpendicular to the defect plane, and as small as possible in the two periodic directions to obtain an irreducible description of the relaxed defect structure.

After relaxing the atomistic structure using a conjugate-gradient minimization procedure, a reference pattern for the crystal defect is derived from the atoms that form the core of the defect. Core atoms are those atoms which could not be classified as lattice atoms by the structure identification method.

3.7. The structure identification algorithm

In this section we give a brief overview of the functionality of the employed structure identification algorithm. Technical details can be found in [14].

The algorithm takes an atomistic reference pattern $\mathscr{L}_\mathrm{P}$ from the structure catalog, and finds all its occurrences in the input configuration $\mathscr{B}$. The specification of a pattern consists of n atoms with the Cartesian coordinates $\mathbf{l}_1, \ldots, \mathbf{l}_n$ and, depending on the dimensionality of the defect or lattice structure, up to three repeat vectors $\mathbf{h}_1, \mathbf{h}_2, \mathbf{h}_3$ that define the geometry of the irreducible periodic cell. If a match between the reference pattern and a group of atoms in $\mathscr{B}$ is found, the search algorithm yields the mapping between the atoms in $\mathscr{B}$ and in $\mathscr{L}_\mathrm{P}$. Note that multiple atoms in $\mathscr{B}$ may be mapped to the same atom in $\mathscr{L}_\mathrm{P}$ when the pattern is periodic. Ultimately, for each nearest-neighbor bond a-b in the matched region of $\mathscr{B}$, we obtain a corresponding interatomic vector $\mathbf{l}_{ab}$ in $\mathscr{L}_\mathrm{P}$.

Note that the rotational symmetries of lattices (and some defects) render the mapping between the reference pattern and the actual crystal non-unique. For instance, in the fcc lattice, the nearest-neighbor vectors comprise the $1/2\,\langle 110\rangle$ vector family in the stress-free unit cell. There are 48 equivalent ways of assigning these vectors to the bonds of an fcc atom, corresponding to the 48 point group symmetry operations of the cubic lattice. We therefore have to make sure that the assignment happens for all atoms in a globally consistent manner, meaning that (i), given any nearest-neighbor pair a-b in $\mathscr{B}$, the sum $\mathbf{l}_{ab} + \mathbf{l}_{ba} = \mathbf{0}$ vanishes, and (ii), given any triplet of atoms a, b, c, all three being mutual nearest neighbors, the circular vector sum $\mathbf{l}_{ab} + \mathbf{l}_{bc} + \mathbf{l}_{ca} = \mathbf{0}$ vanishes as well. In other words, the local lattice orientation established at an atomic site is in alignment with the orientations picked at all its neighbors, and, ultimately, throughout the entire crystallite.

3.8. Mapping tessellation edges to the stress-free state

The structural analysis described in the preceding section (and in much greater detail in [14]) maps bond vectors, corresponding to neighbor atom pairs, to the stress-released state. This information must now be carried over to the edges of the superimposed tetrahedral mesh to perform the elastic-plastic decomposition. If a tetrahedral edge connects two atoms which are immediate neighbors in the input configuration $\mathscr{B}$, then the corresponding ideal lattice vector has already been determined by the structure identification algorithm, and we are done. As shown in figure 3, tessellation edges may, however, connect non-nearest neighbor atoms, in particular in the slipped configuration $\mathscr{B}_1$ where a tetrahedron may become elongated if cut by a dislocation, letting its corner atoms move further apart. The ideal lattice vector of such a long edge, a-c, can be computed by finding a nearest-neighbor path $a \to b_1 \to \ldots \to b_n \to c$ through the crystal that connects the two edge vertices. The total vector $\mathbf{l}_{ac}$, describing the relative position of atoms a and c in the stress-free configuration, is then obtained by summing up the ideal bond vectors in the path, i.e. $\mathbf{l}_{ac} = \mathbf{l}_{ab_1} + \mathbf{l}_{b_1 b_2} + \ldots + \mathbf{l}_{b_n c}$. One can use shortest-path search algorithms such as Dijkstra's algorithm [5] to find a sequence of nearest-neighbor bonds connecting two distant atoms in the lattice. In section 3.11 we will discuss the complications that may arise from nearby dislocations, which make the resulting vector sum path-dependent.

Now that the tetrahedral edge vectors have been determined for each of the configurations $\mathscr{B}_0$, $\mathscr{L}_0$, $\mathscr{B}_1$ and $\mathscr{L}_1$, we compute the element-wise elastic and plastic deformation tensors as described in section 3.3.

3.9. Lattice symmetries and rigid-body rotations

If the crystal lattice possesses rotation or inversion symmetries, care must be taken when choosing the two isoclinic intermediate configurations $\mathscr{L}_0$ and $\mathscr{L}_1$. For cubic crystal structures, for instance, 48 equivalent choices for the isoclinic configurations exist, corresponding to the 48 elements of the space group.

Let us assume that such a crystal undergoes a rigid-body rotation only ($\mathbf{F} = \mathbf{R}$). To perform the elastic-plastic decomposition, we may pick any frame of reference for $\mathscr{L}_0$ which is aligned with the atomic lattice from the set of equivalent lattice orientations. $\mathscr{L}_1$, however, must be chosen such that the computed plastic slip tensor, $\mathbf{F}^{\mathrm{s}}$, becomes identity. This is achieved as follows: The algorithm first picks some trial orientation for the second isoclinic configuration, $\mathscr{L}_1$, from the lattice's point symmetry group. It then searches the crystallite for a local group of atoms (i.e. an atom and its nearest neighbors), which has not undergone any plastic deformation. This is checked by verifying that the central atom is still surrounded by the same set of neighbor atoms in the final configuration (using their unique identifiers) and that the transformation matrix $\mathbf{F}^{\mathrm{s}}_{*}$, exactly mapping all its neighbor bonds from configuration $\mathscr{L}_0$ to $\mathscr{L}_1$, is in fact an element of the lattice's symmetry group.

The inverse of this transformation matrix is then applied to the initial choice for the intermediate configuration $\mathscr{L}_1$ to "align" it with $\mathscr{L}_0$. In particular, this will let the plastic deformation gradient $\mathbf{F}^{\mathrm{s}}_{*}$, computed for the rigid group of atoms above, become identity. Note that the described alignment of the two isoclinic intermediate configurations needs to be performed only once for each crystallite in the simulation (each *super cluster* according to [14]), and not for every tessellation element.

3.10. Limitations

The described computational decomposition of the deformation gradient relies on our ability to predict what the shape of a tetrahedral element would be in the absence of stresses. To this end, we used a structure identification method to first determine the lattice or defect structure formed by the local group of atoms (in configuration $\mathscr{B}$), and, on this basis, project what their (relative) positions would be in the ideal, stress-free configuration $\mathscr{L}$. Conversely, we will be unable to perform the elastic-plastic decomposition if the identification algorithm fails to identify the atomic structure in the first place. This may happen for three reasons:

(i) The atoms form an amorphous phase without long-range order. Then there is no practical way of predicting what the arrangement of atoms would be in the absence of external stress fields (other than performing the relaxation procedure described in section 3.4 explicitly). Hence, our approach is not applicable to disordered systems.

(ii) The crystalline (defect) structure formed by atoms cannot be identified by the structure identification algorithm because it is not covered by the structure catalog. Clearly, not all possible defective arrangements of atoms can be anticipated in practice. One example for such structures are unstructured (general) grain boundaries. However, our method's inability to capture plastic deformation in such crystal defects can, for some applications, be turned into an advantage when it comes to the quantification of competing plastic deformation mechanisms: If the total plastic deformation of a specimen can be measured by other means, for instance by unloading the material and measuring

the irreversible macroscopic strain, then the contribution of non-dislocation deformation mechanisms can be estimated from the difference of the total plastic strain and the slip-based strain measured with our method. A similar approach has been applied in [17] to quantify the contribution of grain boundary sliding to plastic deformation in nanocrystalline metals.

(iii) The random thermal displacements of atoms (in an instantaneous MD simulation snapshot) are too large and exceed the tolerance of the structure identification method. This is a technical issue, which largely depends on the sensitivity of the employed structure analysis method. For instance, the common neighbor analysis occasionally fails to classify the bond structure of atoms at elevated temperatures. Usually this effect pertains only to single atoms in the crystal, while the bulk of atoms are classified correctly. Then it is possible to infer the ideal bond vectors of unidentified atoms from the known bond vectors of their neighbors (e.g., $\mathbf{l}_{ab}$ gives $\mathbf{l}_{ba} = -\mathbf{l}_{ab}$, and $\mathbf{l}_{ab}$ and $\mathbf{l}_{ac}$ give $\mathbf{l}_{bc} = \mathbf{l}_{ac} - \mathbf{l}_{ab}$).

3.11. Dislocations

In sections 2.2 and 3.3, we described the general principle for calculating a deformation gradient field from atomistics. The key device is the space-filling tessellation, which connects the same atoms in the reference, the first intermediate, the second intermediate and the final configuration. We can regard the edges of the tessellation mesh as small line elements, which are transformed by the calculated local deformation tensors from one configuration to another. While each tetrahedron posses six edges, only three non-coplanar line elements (edges) are required to compute a local transformation tensor. In regions of the crystal where the elastic deformation field is compatible, it does not matter which three edges we pick out of the six available edges per tetrahedron. Any combination would give the same tensor.

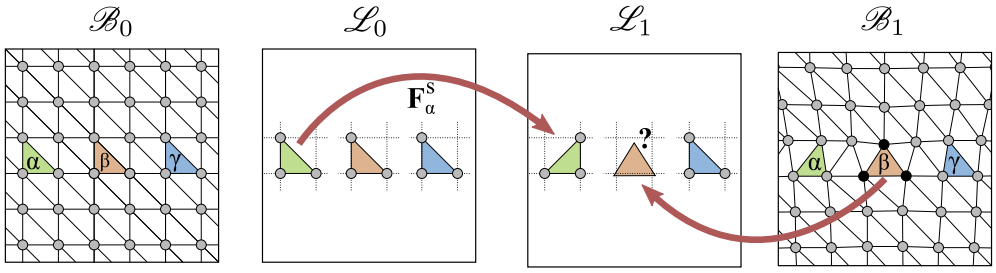

Figure 5. Three tessellation elements (α, β and γ) are shown in the initial and final configurations, $\mathscr{B}_0$ and $\mathscr{B}_1$, with the latter containing a dislocation. Each edge of the tessellation mesh is mapped to the intermediate lattice configurations $\mathscr{L}_0$ and $\mathscr{L}_1$. As element β is located inside the core region of the dislocation in $\mathscr{B}_1$ (marked by the three black atoms), its shape in $\mathscr{L}_1$ is ambiguous. Even if we individually map the three edges that bound element β to the ideal configuration they would no longer form a closed triangle (closure failure). In other words, the three edges of element β form a minimal Burgers circuit around the mathematical dislocation line, and the local elastic field is multi-valued.

In the vicinity of a dislocation, however, the elastic field is incompatible (or multi-valued) and the mapping of interatomic bonds to an ideal lattice is ambiguous as shown in figure 5. Note that this picture is somewhat misleading since, in practice, we map tessellation edges (line elements), and not atomic positions, from the spatial

configuration $\mathscr{B}$ to the associated stress-free configuration $\mathscr{L}$. This means that, inside the dislocation core, where tessellation elements suffer from a closure failure, our choice of the three non-coplanar edges will determine the obtained elastic tensors when evaluating equation 9 or 10 respectively. This ambiguity is connected to the fact that the exact location of the mathematical dislocation line is not precisely defined at the atomic level. The uncertainty in the dislocation position leads to an unknown plastic deformation increment, which is bounded by the product of the Burgers vector and the diameter of the tessellation element intersected by the dislocation line. Usually, this error is rather small in comparison to the macroscopic plastic flow and can therefore be neglected. In practice, we pick three edges at random for each tetrahedron to perform the elastic-plastic decomposition. Thus, any local uncertainty errors resulting from the incompatibility of the elastic field will be averaged out when integrating the field over the simulation domain to obtain the macroscopic plastic deformation.

4. Examples

We have implemented the described elastic-plastic decomposition method in an analysis computer code for atomistic simulation data. The code takes two simulation snapshots and a set of stress-free structure patterns as input. It outputs the computed fields $\mathbf{F}$, $\mathbf{F}^{\Delta\mathrm{e}}$ and $\mathbf{F}^{\Delta\mathrm{p}}$ on the tessellation mesh in addition to their macroscopic, volume-averaged values. In the following we present two exemplary results obtained with this analysis tool.

4.1. Sheared single crystal

To verify the method, we have simulated the shear deformation of a Cu single crystal at T=300 K. As shown in figure 6, the initial configuration $\mathscr{B}_0$ is a perfect fcc crystal in a periodic simulation box, with the (112), $(1\bar{1}0)$, and $(11\bar{1})$ crystal directions aligned with the Cartesian axes x, y and z respectively. The crystal is deformed at a fixed shear rate of 10^9/s by continuously varying the shape of the periodic simulation cell ($(112)\,[11\bar{1}]$ simple shear).

At about 12% (fully elastic) macroscopic shear strain, the maximum strength of the material is reached and the crystal slips by homogeneous nucleation of partial dislocation loops on parallel $[11\bar{1}]$ planes. Several loops are nucleated in a rapid sequence on adjacent crystal planes, resulting in several twinned regions as well as stacking faults in the material. A large drop in the measured shear stress can be observed, after which the stress rises again until one of the twin boundaries starts to migrate at about 20% total shear strain, resulting in a second drop in the measured stress.

The structure catalog used for this deformation field analysis comprises three patterns: The fcc primitive cell (one atom), the irreducible unit cell of intrinsic stacking faults (two core atoms), and the irreducible unit cell of coherent twin boundaries (one core atom). Figure 6 shows a cross-sectional view of the total, plastic and elastic deformation gradient fields at the end of the simulation. The shear component of the plastic deformation field is exactly zero in regions of the crystal that did not undergo slip, and exhibits a large value in the faulted and twinned regions. The elastic field, in contrast, has a uniform, non-zero value throughout the entire crystal. The microscopic elastic field is superposed with random thermal noise at the atomic scale.

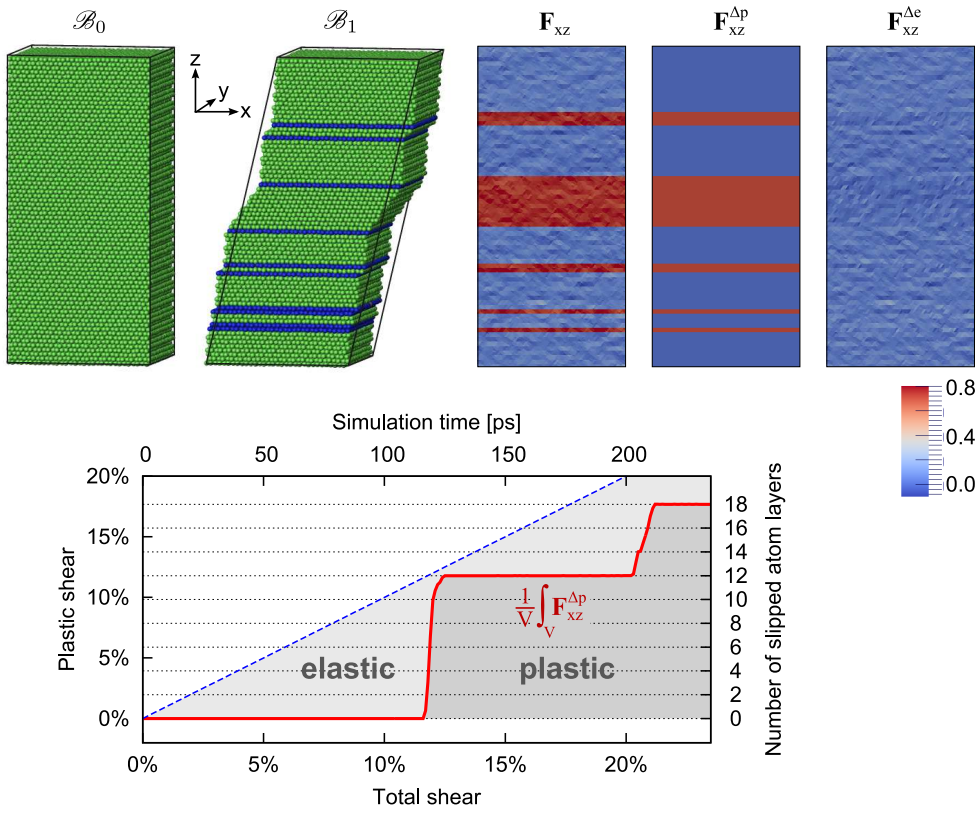

Figure 6. Molecular dynamics simulation of a sheared single crystal, serving as a test for the presented elastic-plastic decomposition method. Top left: The initial and the final configuration of the atomistic system. Top right: Visualization of the shear component of the fields $\mathbf{F}$, $\mathbf{F}^{\Delta e}$ and $\mathbf{F}^{\Delta p}$ as computed with the described method. Bottom: Plot of the instantaneous, volume-averaged value of the measured plastic shear deformation field as a function of total deformation.

The averaged plastic shear magnitude, i.e. the integral $1/V \int F_{xz}^{\Delta p} \mathrm{d}V$ over the entire simulation domain, has been plotted as a function of the total deformation. As expected, the measured plastic shear never exceeds the current total shear, and rises in fixed increments, corresponding to fully slipped crystal planes. Each slipped {111} atomic layer contributes $\delta = \sqrt{1/2}/N$ of plastic shear strain, with N being the total number of {111} layers in the periodic simulation cell.

4.2. Nanoindentation simulation

We have applied the deformation field analysis to an MD simulation of a Cu thin film nanoindentation experiment (figure 7). The simulation box (about 45 nm wide in each direction) contains 7.5 million atoms initially arranged on a fcc lattice. Periodic boundary conditions are applied in the in-plane directions of the thin film. At the bottom of the simulation box, several atomic layers are fixed to provide a rigid support. The spherical indentor (radius 8.7 nm, modeled by an external force field) is pushed into the {111} crystal surface with a constant velocity of 20 m/s. The temperature of the system remains close to 0 K during the entire simulation.

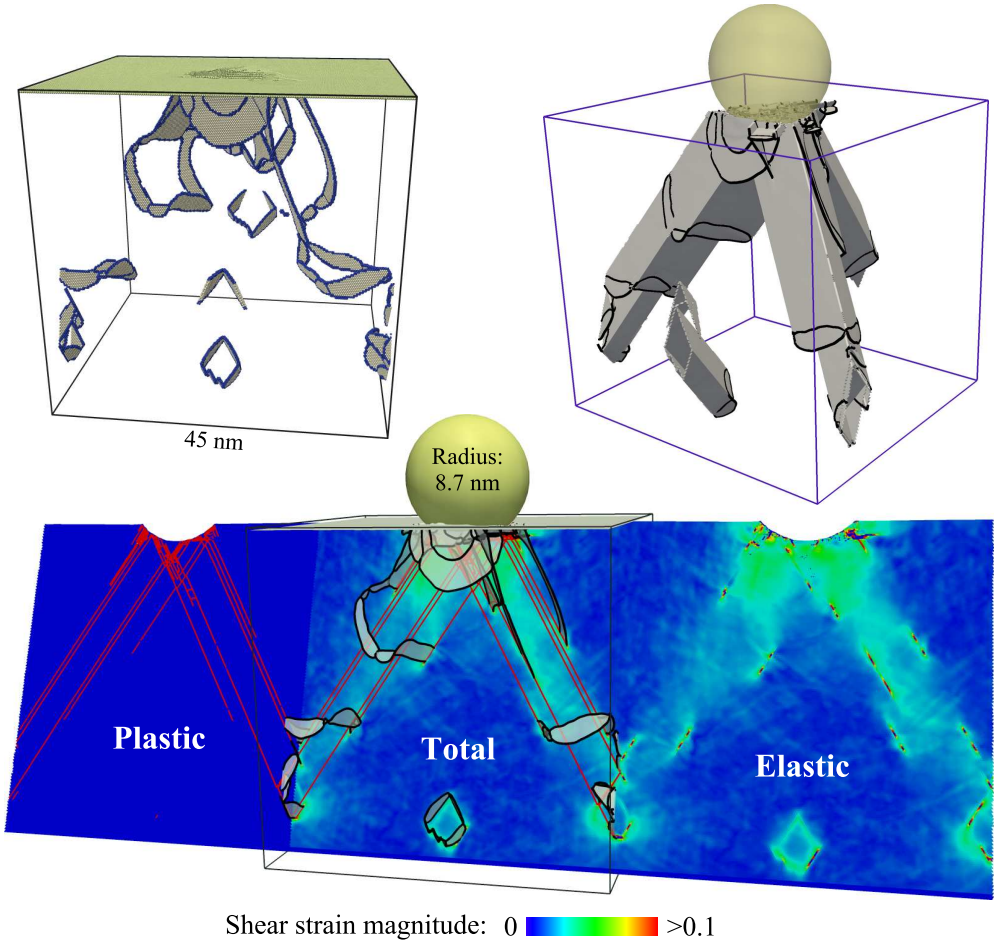

Figure 7. Molecular dynamics simulation of a nanoindentation experiment. Top left: Atomistic visualization of the dislocation structure beneath the indentation site. Only atoms in defective arrangements are shown, while atoms with a perfect fcc environment have been removed. Top right: Three-dimensional contour plot of the plastic zone, showing only tessellation elements with non-zero plastic shear strain magnitude (dislocation slip traces). Bottom: Cross-sectional view of the deformation field. Colors visualize the local shear magnitude. The total deformation field (center) has been decomposed into a plastic part (left) and an elastic part (right). Black lines indicate the position of the prismatic dislocation loops, which intersect the cross-section plane.

We have analyzed a snapshot of the MD simulation taken after 0.132 ns, corresponding to an indentation depth of 2.6 nm. The upper left picture visualizes the state of the atomistic system, in which only atoms in non-fcc arrangements are shown to reveal the dislocation structure. Figure 7 shows a cross-section of the deformation field beneath the indentor derived from the atomic displacements. The Delaunay tessellation [1, 3], generated for the deformation field analysis, comprises about 45 million tetrahedral cells. We have plotted the second invariant of the inverse of the left Cauchy-Green tensor, $\mathbf{c} = \mathbf{F}^{-T}\mathbf{F}^{-1}$, being a measure of the local shear strain magnitude in the current configuration. In addition, we used the dislocation extraction

algorithm (DXA) [15] to obtain a geometric line representation of the dislocations in the plastic zone.

During indentation, several prismatic dislocation loops of increasing size are nucleated beneath the indentor and move along three different $\langle 111 \rangle$ directions into the material. The indentor impact and the gliding dislocations produce elastic waves that are reflected at the rigid substrate, and which are visible in the instantaneous deformation field.

The total deformation field has been decomposed into elastic and plastic parts using the computational method described in this paper. This corresponds to separating the slip traces of dislocations (plastic) from the intrinsic dislocation strain fields, the phonons, and the external indentor field (all elastic). In the upper right picture, only tessellation tetrahedra with non-zero plastic shear strain are displayed to visualize the three-dimensional trajectories of prismatic dislocation loops.

5. Summary

In classical molecular dynamics simulations, the elastoplastic deformation behavior of materials emerges solely from the interactions of individual particles. In particular, defects such as dislocations are not modeled explicitly. Therefore, it is not obvious how to quantify plastic deformation in such simulations and to separate it from elastic deformation.

In the present work, we propose a computational analysis method that enables the separation of incremental elastic and plastic deformation at the atomic level based on two snapshots of the simulated system. Our method allows us to measure the overall plastic strain produced by moving dislocations and other defects and to obtain a continuum field description of the elastic and plastic deformation. Thus, we devised a practical method to calculate the continuum quantities $\mathbf{F}$, $\mathbf{F}^{\mathrm{e}}$, and $\mathbf{F}^{\mathrm{p}}$ from the motion of particles in an atomistic system.

Our consideration of the classical definition of elastic-plastic decomposition in a continuum showed that it is not directly applicable to analyses at the atomic level. Acknowledging these practical difficulties, our goal was to develop a useful technique that yields sensible results for a wide range of crystalline systems if they deform by crystal slip mechanisms, in particular by the motion of dislocations and coherent crystal interfaces.

It should be noted that our approach to measure plastic deformation is of kinematic nature and does not require an explicit relaxation or unloading of the atomic structure to a stress-free state, nor does it involve the concept of stress at the atomic level. Thus, the described analysis method is efficient, does not depend on the interaction model employed in an atomistic simulation, and is not restricted to certain crystal structures. It can be incorporated into existing molecular dynamics codes to enable on-the-fly measurements of the inelastic deformation of a crystalline system, complementing the classical stress-strain curve measurement. Another possibility is to perform plastic strain rate measurements, by comparing successive snapshots taken at regular time intervals. By numerical differentiation of the incremental strains, one can obtain the elastic and plastic strain rates of the deforming system.

Acknowledgments

The authors thank B. Eidel and J. Zimmerman for helpful comments. This work was performed under the auspices of the U.S. Department of Energy by Lawrence Livermore National Laboratory under Contract DE-AC52-07NA27344.

References

[1] CGAL, Computational Geometry Algorithms Library. Available at http://www.cgal.org/.

[2] G. J. Ackland and A. P. Jones. Applications of local crystal structure measures in experiment and simulation. *Phys. Rev. B*, 73(5):054104, 2006.

[3] J.-D. Boissonnat, O. Devillers, S. Pion, M. Teillaud, and M. Yvinec. Triangulations in CGAL. *Computational Geometry*, 22:5–19, 2002.

[4] C. Davini. A proposal for a continuum theory of defective crystals. *Archive for Rational Mechanics and Analysis*, 96:295–317, 1986.

[5] E. W. Dijkstra. A note on two problems in connexion with graphs. *Numerische Mathematik*, 1:269–271, 1959.

[6] F. C. Frank. LXXXIII. Crystal dislocations – Elementary concepts and definitions. *Philosophical Magazine Series 7*, 42(331):809–819, 1951.

[7] P. M. Gullett, M. F. Horstemeyer, M. I. Baskes, and H. Fang. A deformation gradient tensor and strain tensors for atomistic simulations. *Model. Simul. Mater. Sci. Eng.*, 16(1):015001, 2008.

[8] J. D. Honeycutt and H. C. Andersen. Molecular dynamics study of melting and freezing of small Lennard-Jones clusters. *J. Phys. Chem.*, 91(19):4950–4963, 1987.

[9] E. H. Lee. Elastic-plastic deformation at finite strains. *J. Appl. Mech.*, 36:1–6, 1969.

[10] J. Mandel. Plasticité classique et viscoplasticité. *CISM course No. 97, Springer*, 1971.

[11] P. H. Mott, A. S. Argon, and U. W. Suter. The atomic strain tensor. *J. Comput. Phys.*, 101(1):140–150, 1992.

[12] S. Nemat-Nasser. Decomposition of strain measures and their rates in finite deformation elastoplasticity. *International Journal of Solids and Structures*, 15 (2):155–166, 1979.

[13] F. Shimizu, S. Ogata, and J. Li. Theory of shear banding in metallic glasses and molecular dynamics calculations. *Mater. Trans.*, 48(11):2923–2927, 2007.

[14] A. Stukowski. Structure identification methods for atomistic simulations of crystalline materials. Submitted to Modelling Simul. Mater. Sci. Eng.

[15] A. Stukowski and K. Albe. Extracting dislocations and non-dislocation crystal defects from atomistic simulation data. *Modelling Simul. Mater. Sci. Eng.*, 18 (8):085001, 2010.

[16] C. Teodosiu and F. Sidoroff. A theory of finite elastoviscoplasticity of single crystals. *International Journal of Engineering Science*, 14(2):165–176, 1976.

[17] N. Q. Vo, R. S. Averback, P. Bellon, S. Odunuga, and A. Caro. Quantitative description of plastic deformation in nanocrystalline Cu: Dislocation glide versus grain boundary sliding. *Phys. Rev. B*, 77(13):134108, 2008.

[18] J. A. Zimmerman, C. L. Kelchner, P. A. Klein, J. C. Hamilton, and S. M. Foiles. Surface step effects on nanoindentation. *Phys. Rev. Lett.*, 87(16):165507, 2001.

[19] J. A. Zimmerman, D. J. Bammann, and H. Gao. Deformation gradients for continuum mechanical analysis of atomistic simulations. *Int. J. Solids Struct.*, 46 (2):238–253, 2009.